ACS APPLIED MATERIALS & INTERFACES

www.acsami.org

Research Article

# Bication-Mediated Quasi-2D Halide Perovskites for High-Performance Flexible Photodetectors: From Ruddlesden–Popper Type to Dion–Jacobson Type

Zhengxun Lai, Ruoting Dong, Qi Zhu, You Meng, Fei Wang, Fangzhou Li, Xiuming Bu, Xiaolin Kang, Heng Zhang, Quan Quan, Wei Wang, Feng Wang, SenPo Yip, and Johnny C. Ho*

Cite This: *ACS Appl. Mater. Interfaces* 2020, 12, 39567–39577

Read Online

ACCESS | Metrics & More | Article Recommendations | Supporting Information

**ABSTRACT:** Quasi-2D halide perovskites, especially the Ruddlesden–Popper perovskites (RPPs), have attracted great attention because of their promising properties for optoelectronics; however, there are still serious drawbacks, such as inefficient charge transport, poor stability, and unsatisfactory mechanical flexibility, restricting further utilization in advanced technologies. Herein, high-quality quasi-2D halide perovskite thin films are successfully synthesized with the introduction of the unique bication ethylenediammonium (EDA) via a one-step spin-coating method. This bication EDA, with short alkyl chain length, can not only substitute the typically bulky and weakly van der Waals-interacted organic bilayer spacer cations forming the novel Dion–Jacobson phase to enhance the mechanical flexibility of the quasi-2D perovskite (e.g., $EDA(MA)_{n-1}Pb_nI_{3n+1}$; MA = $CH_3NH_3^+$) but also serve as a normal cation to achieve the more intact films (e.g., $(iBA)_2(MA)_{3-2x}(EDA)_xPb_4I_{13}$). When fabricated into photodetectors, these optimized EDA-based perovskites deliver an excellent responsivity of 125 mA/W and a fast response time down to 380 $\mu$s under 532 nm irradiation. More importantly, the device with the Dion–Jacobson phase perovskite can be bent down to a radius of 2 mm and processed with 10,000 cycles of the bending test without any noticeable performance degradation because of its superior structure to RPPs. Besides, these films do not exhibit any material deterioration after ambient storage for 30 days. All these performance parameters are already comparable or even better than those of the state-of-the-art RPPs recently reported. This work provides valuable design guidelines of the quasi-2D perovskites to obtain high-performance flexible photodetectors for next-generation optoelectronics.

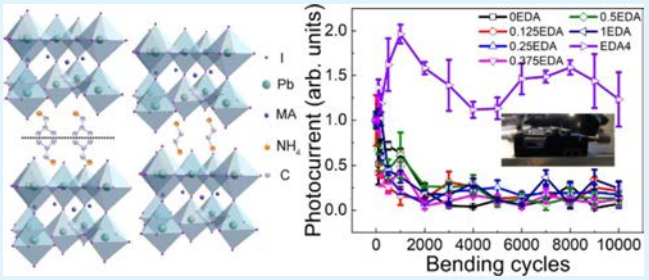


**KEYWORDS:** *Ruddlesden–Popper phase, Dion–Jacobson phase, halide perovskite, EDA, photodetector, flexible device*



## INTRODUCTION

In recent years, three-dimensional (3D) organic–inorganic halide perovskites, such as $MAPbI_3$ (MA = $CH_3NH_3^+$), have attracted significant research attention because of their high performance in optoelectronic devices.[1−8] For example, the power conversion efficiency of $MAPbI_3$-based solar cells has already exceeded 24% in the latest development,[9−12] which is promising to compete with mainstream silicon solar cells in the near future. However, the stability of conventional 3D halide perovskites is quite poor, where the devices can be easily degraded in an ambient atmosphere.[13,14] One effective way to tackle this stability issue is to insert large-scale organic molecules, including $CH_3(CH_2)_3NH_3^+$ (butylamine, BA) and $C_6H_5(CH_2)_2NH_3^+$ (phenethylammonium, PEA), into the perovskites to form the two-dimensional (2D) or quasi-2D Ruddlesden–Popper phase, that is, Ruddlesden–Popper perovskites (RPPs).[15−18] In general, the chemical formula of RPPs can be written as $L_2A_{n-1}B_nX_{3n+1}$ such that L represents the large-scale organic spacer cation, A and B designate the regular cations located at the corner and body center of the crystal lattice, respectively, and X refers to the halide positioned at the face center. Thus, for the case of $L_2A_{n-1}B_nX_{3n+1}$, the $A_{n-1}B_nX_{3n+1}$ unit is sandwiched between two L cation layers.[19,20] The variable n is an integer, representing the number of metal halide octahedral layers between the two L cation layers. To date, there have been many extensive studies on RPPs for the enhanced device performance. To be specific, Smith and his co-workers achieved the high-quality $(PEA)_2(MA)_2Pb_3I_{10}$ films by spin coating,[21] which is a simple material synthesis scheme applicable to almost all RPPs. Later, Cao et al. optimized the

Received: May 27, 2020
Accepted: August 7, 2020
Published: August 7, 2020




https://dx.doi.org/10.1021/acsami.0c09651
*ACS Appl. Mater. Interfaces* 2020, 12, 39567–39577

spin-coating fabrication method to obtain a series of $(BA)_2(MA)_{n-1}Sn_nI_{3n+1}$ films with controllable optical band gaps, in which their moisture stability was demonstrated to be much better than that of 3D counterparts.[22] Although the inserted large-scale organic molecules of RPPs can considerably improve their ambient stability, these organic molecules would inevitably also serve as insulating barriers, substantially decreasing the optoelectronic performance and thermal stability.[23] Hence, the smaller L is highly preferred for the spacer cation. In this view, $^+NH_3(CH_2)_2NH_3^+$ (ethylenediammonium, EDA) is an ideal organic molecule here with almost the shortest alkyl chain separating the metal halide octahedral layers.[24] Notably, because there are two $NH_4^+$ in each EDA cation, one EDA layer is sufficient to function as the spacer cations rather than two BA or two PEA layers (i.e., organic bilayers) required in the conventional RPPs, which can ultimately decrease the thickness of the spacer layer. This kind of quasi-2D perovskites with only one layer as the spacer cation is called Dion–Jacobson phase-layered perovskites (DJPs).[25] Besides, because of the relatively short chain of EDA, it can also substitute MA in the halide perovskite. At present, although several groups have reported the synthesis of perovskites with a small amount of EDA partially substituting MA,[26,27] there are still very limited systematic studies on EDA as the spacer cation for DJPs.[28,29] In any case, it is highly beneficial to integrate EDA cations into halide perovskites for the further performance and stability enhancement of perovskite optoelectronic devices, with more detailed studies urgently needed.

In this work, high-quality organic–inorganic halide perovskite films with the integration of bication EDA are successfully synthesized by the one-step spin-coating process, either sitting in the spacer site (serving as the spacer layer) or the cation (A) site or both. When EDA is employed as the spacer cation (DJPs), the $EDA(MA)_{n-1}Pb_nI_{3n+1}$ films with $n$ ranging from 1 to 4 are achieved and configured into both rigid and flexible photodetectors. These devices can deliver an impressive responsivity of 125 mA/W and efficient rise and decay times down to 410 and 380 $\mu$s, respectively, under 532 nm irradiation. The fabricated flexible photodetectors give superior mechanical bending performance as compared with the RPP devices, which can be attributed to the vanishing of weak van der Waals interactions between organic bilayers derived from the unique bication EDA. On the other hand, once EDA is put in the cation (A) site, the $n$ = 4 RPP films of $(iBA)_2(MA)_{3-2x}(EDA)_xPb_4I_{13}$ with $x$ spanning from 0 to 1.5 are synthesized. It is interesting that as $x$ increases, the flexibility and moisture stability of fabricated RPP photodetectors are obviously enhanced, although the responsivity decreases gradually at a cost. The transient response time of all these RPP devices with EDA as cations is determined to be lower than 440 $\mu$s, even being already comparable to some of the single-crystal halide perovskite photodetectors. All these remarkable results would pave a promising way to break the bottleneck of the research and applications of quasi-2D perovskites and other halide perovskites.

## RESULTS AND DISCUSSION

For the typical crystal structure of RPPs, such as $(iBA)_2(MA)_{n-1}Pb_nI_{3n+1}$, the $(MA)_{n-1}Pb_nI_{3n+1}$ layer is sandwiched between two *i*BA organic layers, where n represents the layer number of $PbI_6$ octahedra stacked along the c axis, where the crystal structure of $n$ = 2 is chosen as an illustrative example, as shown in Figure 1a. In fact, the bonding between these two *i*BA organic layers comes from the weak van der

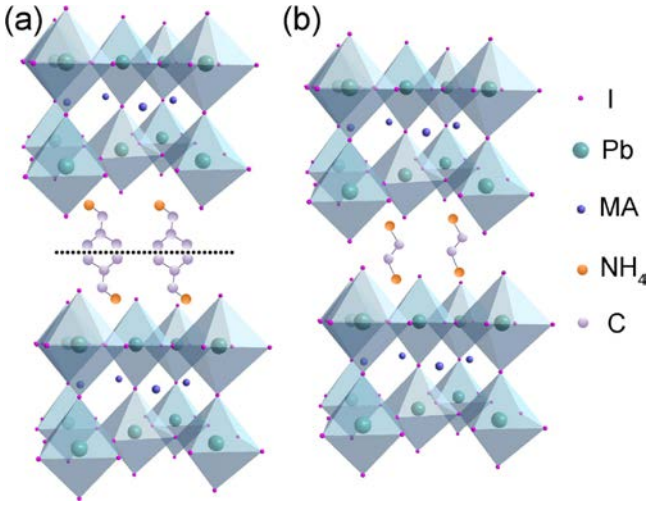


**Figure 1.** Schematic illustration of the crystal structure of the RPP (a) $(iBA)_2MAPb_2I_7$ and Dion–Jacobson perovskite (b) $EDAMAPb_2I_7$.

Waals interaction that is marked with a dotted line in the figure.[30] In contrast, when bication EDA served as the spacer cation, as given in Figure 1b, there is only one EDA molecule needed for each spacer layer; therefore, this spacer of DJPs becomes much thinner than those of RPPs. Moreover, if EDA is exploited as the normal A-site cation, the cation $MA^+$ in RPPs would be substituted by $EDA^{2+}$ such that two $MA^+$ are able to be replaced by only one $EDA^{2+}$, accordingly, for a more compact structure. Here, the quasi-2D perovskite films with the controlled site occupation of EDA can be fabricated reliably in a one-step spin-coating process. The experimental details can be found in the Experimental Section. The films with the EDA spacer are described, with the chemical formula $EDA(MA)_{n-1}Pb_nI_{3n+1}$ ($n$ = 1, 2, 3, and 4), as EDA1, EDA2, EDA3, and EDA4, respectively. The films with two $MA^+$ substituted by $EDA^{2+}$ are then labeled, with the chemical formula $(iBA)_2(MA)_{3-2x}(EDA)_xPb_4I_{13}$ ($x$ = 0, 0.125, 0.25, 0.375, 0.5, 1, and 1.5), as 0EDA, 0.125EDA, 0.25EDA, 0.375EDA, 0.5EDA, 1EDA, and 1.5EDA, correspondingly, in which the n value of RPPs is fixed at 4 and the *i*BA spacer cation is employed. Besides, we designate the DJPs films of $EDA(MA)_{n-1}Pb_nI_{3n+1}$ and RPP films of $(iBA)_2(MA)_{3-2x}(EDA)_xPb_4I_{13}$ to Group 1 and Group 2 samples, respectively, for simplicity for the rest of the investigation.

In order to evaluate the composition of fabricated perovskite films, X-ray diffraction (XRD) spectra of all the samples were first measured. Figure 2a depicts the XRD pattern of Group 1 samples, where the peaks of $EDA(MA)_{n-1}Pb_nI_{3n+1}$ with $n$ = 1, 2, 3, and 4 are indexed with the black, red, blue, and pink numbers with brackets, respectively. For the case of EDA1, the XRD pattern is observed to be consistent with the $EDAPbI_4$ film reported in the previous work.[24] Because there is no MA present in EDA1, the pure $EDAPbI_4$ film can be acquired. For the XRD spectra of EDA2, EDA3, and EDA4, there are the typical peaks of (110) and (220) planes located at about 14 and 28°, respectively. One can also notice the split of peaks of (110) and (220) planes for both EDA2 and EDA3, which can be caused by the emergence of the coexistence of perovskites


https://dx.doi.org/10.1021/acsami.0c09651
ACS Appl. Mater. Interfaces 2020, 12, 39567–39577

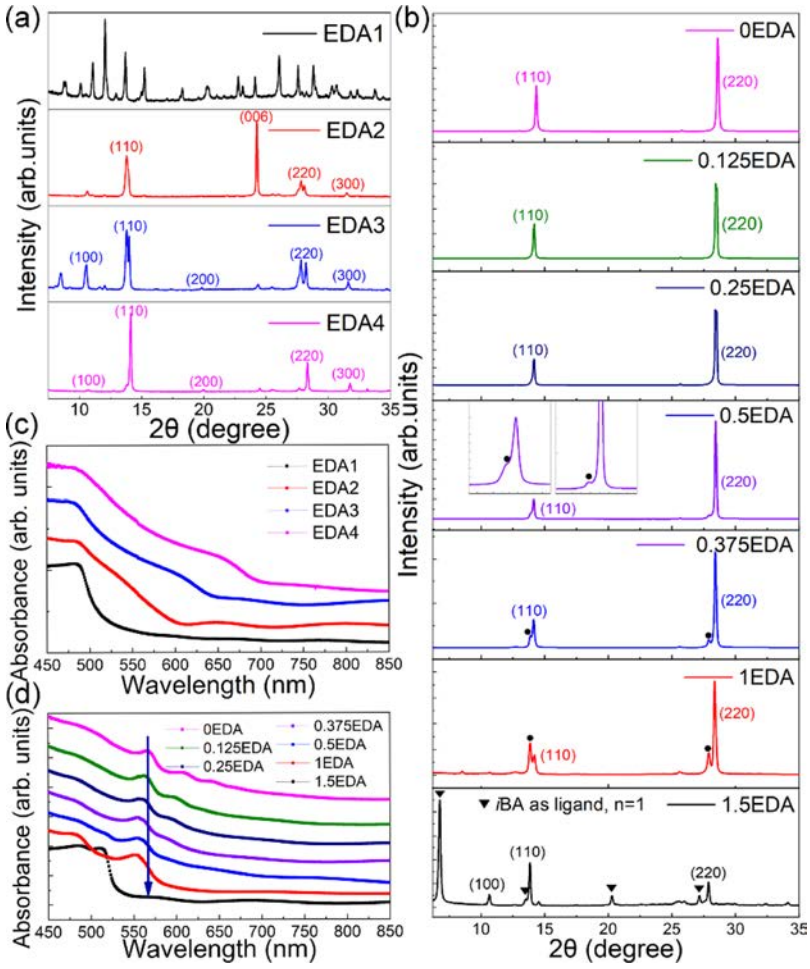


**Figure 2.** (a) XRD spectra of the thin-film samples of $EDA(MA)_{n-1}Pb_nI_{3n+1}$. When $n$ varies from 1 to 4, they stand for the samples of EDA1, EDA2, EDA3, and EDA4 (Group 1 samples). (b) XRD patterns of the thin-film samples of $(iBA)_2(MA)_{3-2x}(EDA)_xPb_4I_{13}$. As $x$ changes from 0 to 1.5, they refer to the samples of 0EDA, 0.125EDA, 0.25EDA, 0.375EDA, 0.5EDA, 1EDA, and 1.5EDA, accordingly (Group 2 samples). (c) Absorption spectra of Group 1 samples. (d) Absorption spectra of Group 2 samples.

with MA and EDA as normal cations. It is known that when the value of n decreases, the amount proportion of spacer molecules (EDA) would increase accordingly; this way, some of the EDA can easily come to act as the normal cations. For this reason, the peak splitting phenomenon is not resulted for EDA4 with a relatively small amount of EDA. Likewise, Figure 2b presents the XRD spectra of Group 2 samples. For the case of 1.5EDA, it is observed to have an additional $n$ = 1 phase with *i*BA as the spacer cation, which is probably because EDA cannot occupy all the cation (A) sites such that the non-A-site phase $n$ = 1 would appear. For the other samples in Group 2, only the typical peaks of (110) and (220) planes are observed, indicating the relatively good phase purity. As the proportion of EDA increases (i.e., from 0.375EDA to 1EDA), the peaks of (110) and (220) planes gradually split into two peaks each, which is possibly related to the phase segregation that one phase consists of the pure EDA cations and another phase comprises the pure MA cations (marked by the black dots in Figure 2b). Figure S1a,b compiles the full width at half-maximum (FWHM) value of the main peaks of the XRD patterns shown in Figure 2a [(110) plane] and b [(220) plane]. For Group 1 samples, the FWHM values of EDA3 and EDA4 are smaller than those of EDA1 and EDA2, indicating better crystallinity of EDA3 and EDA4. For Group 2 samples, as $x$ increases, the FWHM value increases first and then decreases, which suggests that a small amount of EDA partially substituting MA can improve the quality of the samples. To further confirm the differentiation of these structures of RRPs and DJPs, mechanical exfoliation tests were as well performed on the selected samples. As given in Figure S2, the samples of $(iBA)_2PbI_4$ (i.e., using *i*BA as the spacer with $n$ = 1 for the typical RRP material) and 0EDA can be mechanically exfoliated and transferred as flakes onto the $Si/SiO_2$ (270 nm thermal oxide) substrates, while the samples of EDA1 and EDA4 cannot be exfoliated in the same manner with clear evidence of no flake residual on the transfer tapes. This observation suggests that 0EDA has the RRP structure and EDA1 and EDA4 have the DJP structure because 0EDA can be mechanically exfoliated because of the weak van der Waals interaction among its layers but EDA1 and EDA4 do not behave the same.[31,32] At the same time, optical absorption spectra of all the samples were also obtained. Figure 2c gives the absorption spectra of Group 1 samples. In detail, there is only one absorption edge observed at around 500 nm for EDA1, suggesting the pure phase of the sample with a band gap of about 2.48 eV. Particularly, all Group 1 samples display the absorption tails that are probably caused by the small impurities of intergrown higher-order homologous members. For the absorption spectra of Group 2 samples, as illustrated in Figure 2d, when the EDA content increases, the exciton


https://dx.doi.org/10.1021/acsami.0c09651
ACS Appl. Mater. Interfaces 2020, 12, 39567−39577

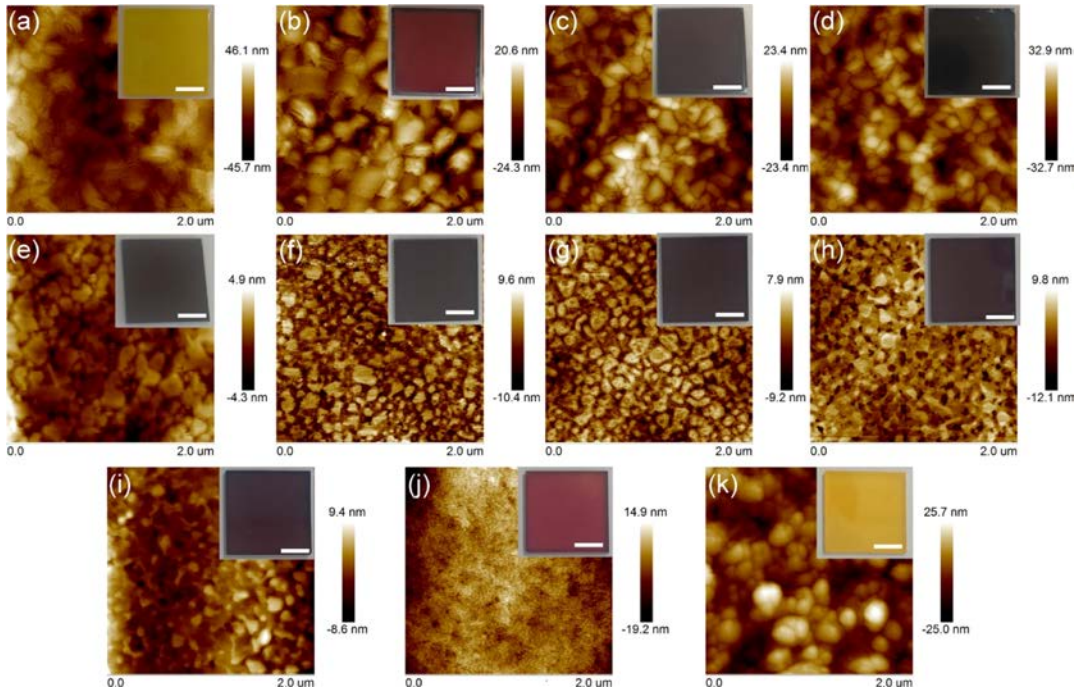


**Figure 3.** Atomic force microscope images of fabricated perovskite films: (a) EDA1, (b) EDA2, (c) EDA3, (d) EDA4, (e) 0EDA, (f) 0.125EDA, (g) 0.25EDA, (h) 0.375EDA, (i) 0.5EDA, (j) 1EDA, and (k) 1.5EDA. All insets show the corresponding optical images, where the scale bar is 5 mm.

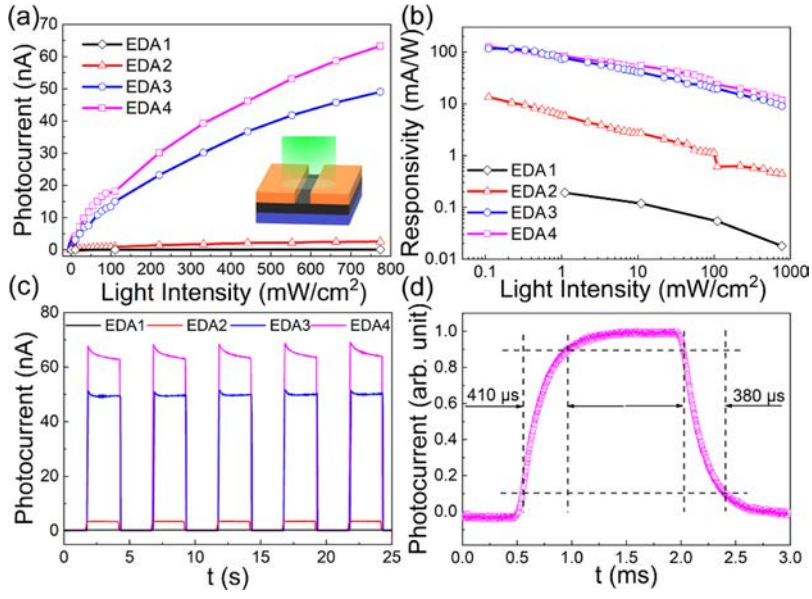


**Figure 4.** Photoresponse properties of fabricated Group 1 devices. (a) Dependence of photocurrent on light intensity, where the inset shows the schematic illustration of the photodetector device structure. (b) Dependence of responsivity on light intensity. (c) Time-dependent photoresponse. (d) High-resolution current vs time curve for the EDA4 device.

absorption peak of fabricated films gives a gradual blue shift, indicating the increasing band gap among the samples. The PL spectra of all the samples were as well investigated. As shown in Figure S3, there are dominant emission peaks observed at about 760 nm for all the Group 1 and Group 2 samples, where the peaks come from the 3D perovskite phase. This result is commonly seen in quasi-2D halide perovskites such that the photogenerated electrons would transfer from the small-*n* to the large-*n* phases, leading to the main emission peak corresponding to $n = \infty$.[33−36] Furthermore, there are additional peaks witnessed at 530 nm for EDA1 and 527 nm for 1.5EDA, which are attributable to the emission from 2D phases of $EDAPbI_4$ and $(iBA)_2(EDA)_{1.5}Pb_4I_{13}$, respectively. All these results evidently demonstrate the effective manipulation of the site occupation of EDA and the corresponding modulation of the band gap of fabricated perovskites.

Apart from the chemical composition and band gap information of the fabricated quasi-2D perovskites, it is also important to assess their morphological features and film conformality. Figure 3a−d shows the atomic force microscopy


https://dx.doi.org/10.1021/acsami.0c09651
ACS Appl. Mater. Interfaces 2020, 12, 39567−39577

(AFM) images of Group 1 samples with the $n$ value changing from 1 to 4, respectively, while Figure 3e−k gives the AFM images of Group 2 samples with the $x$ parameter increasing from 0 to 1.5, accordingly. The insets depict the corresponding optical images of all fabricated films. It is obvious that when n decreases from 4 to 1 for Group 1 samples and $x$ increases from 0 to 1.5 for Group 2 samples, the film color steadily changes from black to yellow. This color change suggests the gradual blue shift of their optical absorption edges, which agree well with the absorption and PL results discussed above. Based on the AFM images, all samples display the compact and uniform morphology without any observable pinholes. The relatively large crystals grains can as well be clearly observed for the obtained films, indicating the good film quality.[37] Notably, the average surface roughness ($R_a$) of perovskite films in Group 1 is found to be 10.5, 5.1, 5.9, and 7.6 nm, respectively, whereas the $R_a$ value of Group 2 samples is within a narrow range of between 1 and 5.6 nm, demonstrating the satisfied film surface roughness and uniformity.[38] Moreover, top-view scanning electron microscopy (SEM) images are also taken to evaluate the large-scale surface morphology of all the DJP and RPP films prepared in Group 1 and Group 2, respectively (Figure S4). These SEM images further confirm the high-quality perovskite films fabricated without any significant concentration of pinholes. The cross-sectional SEM images can then reveal the film thickness of the quasi-2D perovskites. By controlling the spin-coating condition, the film thickness is controlled to about 400−500 nm for all samples. In particular, the typical thickness of the EDA4 film is measured to be 473 nm (Figure S5). In this case, the addition of EDA into the perovskites as either spacer or normal cations would not deteriorate the uniformity and conformality of fabricated films, where these film characteristics are extremely important for the subsequent device fabrication and performance.

Once the high-quality quasi-2D perovskite films are obtained, they can be configured into simple photodetector devices to characterize their photodetection properties. As illustrated in the Figure 4a inset, the device is constructed by depositing two parallel Au electrodes onto the perovskite film predeposited onto the glass substrate with a channel length of 10 $\mu$m. A 532 nm laser is then used as the exciting light for the photodetector measurement. The dependence of photoresponse on the light intensity is first investigated for the Group 1 devices. Based on the photocurrent−voltage ($I$−$V$) characteristics under different light intensities, all devices give the dark current below $3.3 \times 10^{-10}$ A at a voltage bias of 2 V (Figure S6). When the light intensity increases, the output current of all devices also increases, indicating the typical light-sensitive properties of fabricated perovskite films. Importantly, all the $I$−$V$ curves are linear, which suggests the nearly Ohmic contact properties between perovskite films and Au electrodes, being beneficial to the collection of photogenerated carriers. To better understand their photosensing characteristics, the dependence of photocurrent on light intensity is carefully measured and presented in Figure 4a, where the photocurrent is defined as the difference between currents in the dark and under light-illuminated states. It is clear that there is a sublinear relationship witnessed, which is often observed in layered semiconductor-based photodetectors because of the complex processes of electron−hole generation, trapping, and recombination in device channels.[39,40] As the value of n increases from 1 to 4 for the Group 1 samples, the photocurrent is found to increase accordingly. This phenomenon is fully known for the quasi-2D halide perovskite photodetectors because the increasing metal halide octahedral layer number would give the higher effective optical absorption volume for the enhanced photocurrent.[41] Simultaneously, the photoresponsivity ($R$) of all devices is assessed as a function of light intensity and displayed in Figure 4b. $R$ can be analytically described as

$$R = \frac{I_p}{\Phi S} \tag{1}$$

where $I_p$ is the photocurrent, $\Phi$ is the light intensity, and $S$ is the active area of the photodetector. In specific, $R$ is observed to keep increasing with decreasing light intensity. Similar to the results of the photocurrent, the $R$ values of EDA4 and EDA3 are substantially larger than the ones of EDA2 and EDA1, where the largest $R$ of EDA4 can reach 125 mA/W at an intensity of 0.1 mW/cm$^2$. On top of photoresponsivity, detectivity ($D^*$) and external quantum efficiency (EQE) are also important parameters to evaluate the performance of photodetectors. The detectivity and EQE can be defined as $D^* = RS^{1/2}/(2eI_{dark})^{1/2}$ and EQE = $hcR/e\lambda$, where $e$ is the electronic charge, $I_{dark}$ is the dark current of the photodetector, $h$ is Planck's constant, $c$ is the velocity of the incident light, and $\lambda$ is the wavelength of the incident light.[42,43] The $D^*$ and EQE values of Group 1 samples are depicted in Figure S7a,c. When n increases, both $D^*$ and EQE increase accordingly, following the same increasing trend of $R$. The highest $D^*$ and EQE values of EDA4 are found to be $7.1 \times 10^{10}$ Jones and 30%, respectively. In addition, current−time ($I$−$t$) curves under periodical light illumination are also carefully measured to examine the repeatability of fabricated photodetectors, as shown in Figure 4c. These perovskite photodetectors demonstrate the reversible photoswitching characteristics clearly, indicating the excellent stability and photosensing capability of devices. Especially, the EDA4 device exhibits a high photocurrent of 64 nA, a good photoresponsivity of 12 mA/W, and a decent current on/off ratio of $7.5 \times 10^2$ under a relatively high light intensity of 750 mW/cm$^2$. For high-performance photodetectors, fast response speeds are also necessary. As depicted in Figures 4d and S8, high-resolution $I$−$t$ curves are measured, where the rise and decay times of photoresponse are extracted. The rise time is defined as the time interval required for the photocurrent to increase from 10 to 90% of its peak value, while the decay time is from 90 to 10% of the peak value. It is worth mentioning that the rise and decay times are determined to be 410 and 380 $\mu$s, respectively, that have already outperformed most of the other solution-processed halide perovskite devices, being even comparable or better than many single-crystal perovskite-based photodetectors.[4,39,41,44] All these superior performance parameters demonstrate the promising potential of adopting small EDA molecules as spacer cations for the enhancement of RRP photodetectors.

Instead of serving as spacer cations, EDA can as well function as normal cations in Group 2 samples with the fabricated photodetector performance thoroughly evaluated. Figure S9 gives the $I$−$V$ properties of all Group 2 devices measured in the dark and under illumination, where all devices give the dark current below $7.4 \times 10^{-11}$ A at a voltage bias of 2 V. Again, the output current is observed to increase with increasing incident power, illustrating a typical linear relationship with the bias voltage for the evidence of Ohmic-like


https://dx.doi.org/10.1021/acsami.0c09651
ACS Appl. Mater. Interfaces 2020, 12, 39567−39577

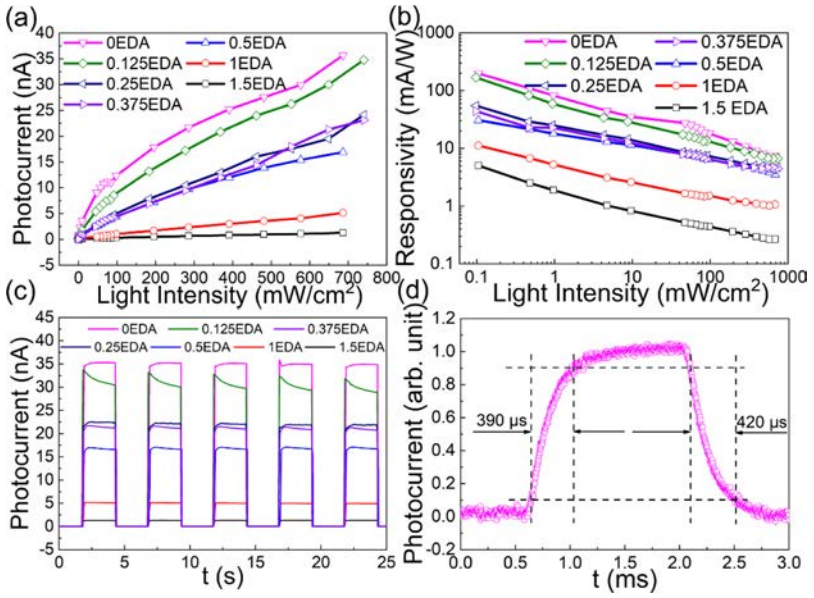


**Figure 5.** Photoresponse properties of fabricated Group 2 devices. (a) Dependence of photocurrent on light intensity. (b) Dependence of responsivity on light intensity. (c) Time-dependent photoresponse. (d) High-resolution current vs time curve for the 0.125EDA device.

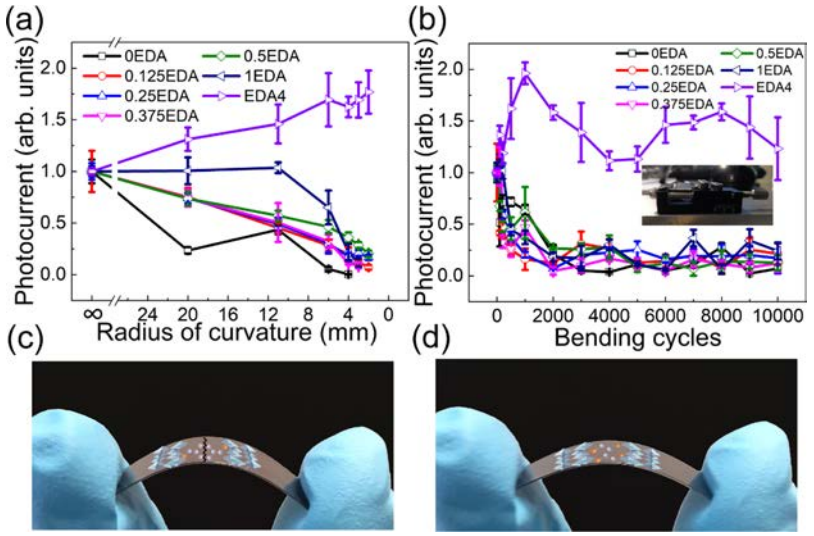


**Figure 6.** (a) Dependence of the normalized photocurrent on the bending curvature of flexible devices, which include the EDA4 and all Group 2 devices. (b) Dependence of the normalized photocurrent on the bending cycles of all flexible devices. The inset shows the optical image of the measurement setup under the bending test. (c) Optical image of the typical RPP film using organic bilayers as the spacer cation under mechanical bending. Schematic of the perovskite crystal structure is illustrated on the film with the potential failure plane depicted along the organic bilayers sandwiched between the two metal halide octahedral layers. (d) Optical image of the EDA4 sample (DJPs) using a single EDA layer as the spacer cation under mechanical bending. Schematic of the perovskite crystal structure is also illustrated on the film, where the more intact structure would make the film have better flexibility as compared to the one depicted in panel (c).

contact here. When the photocurrent is compiled as a function of the light intensity in Figure 5a, the sublinear relationship is illustrated with increasing photocurrent for the decreasing $x$ parameters (i.e., EDA content). The corresponding photoresponsivity is also carefully assessed, as depicted in Figure 5b. The $R$ value is found to be a decreasing function of the light intensity for all devices. The highest $R$ value is determined to be as high as 198 mW/cm$^2$ for the 0EDA device. It is obvious that the photocurrent and photoresponsivity value decrease gradually as the EDA content $x$ increases. It is because of the fact that it is getting more difficult to separate and collect the photogenerated electrons and holes because of the substitution of MA by the bulkier EDA species, which has been demonstrated in RPPs as compared with the 3D counterparts of $MAPbI_3$.[45] The $D^*$ and EQE values of Group 2 samples are also illustrated in Figure S7b,d. When $x$ increases, both $D^*$ and EQE decrease correspondingly, again following the same increasing trend of $R$. The highest $D^*$ and EQE values of 0EDA are determined to be $3.8 \times 10^{11}$ Jones and 46%, respectively. Besides, the photoswitching characteristics of all Group 2 devices are as well measured in the dark and under a light intensity of 750 mW/cm$^2$ (Figure 5c). It is seen that all the mixed cation perovskite devices in Group 2 have the reproducible and stable photoresponses. Particularly, the 0EDA device delivers a photocurrent of 35 nA, a photoresponsivity of 7.4 mA/W, and an on/off ratio of $5.0 \times 10^3$


https://dx.doi.org/10.1021/acsami.0c09651
ACS Appl. Mater. Interfaces 2020, 12, 39567−39577

Table 1. Comparison of Various Figures of Merits of Different RPP (or DJP)-Based Photodetectors

| RPPs (or DJPs) | bias [V] | light (nm) | flexible | $R$ [mA/W] | rise/decay time [ms] | refs |
|---|---|---|---|---|---|---|
| $(BA)_2(MA)_2Pb_3I_{10}$ | 29.3 | 532 | N | 12.78 | 10/7.5 | 41 |
| $(BA)_2(MA)_{n-1}Pb_nBr_{3n+1}$ $(1 < n < \infty)$ crystal | 1 | 500 | N | 190 | 210/240 | 53 |
| $(C_4H_9NH_3)_2PbBr_4$ nanobelt | 5 | 405 | Y | 0.023 | 34/50 | 44 |
| $(PEA)_2PbBr_4$ single crystal | 10 | 365 | N | 31.48 | 0.41/0.37 | 54 |
| $(BA)_2(MA)_3Pb_4Br_{13}$ nanowire | 5 | 530 | N | $1.5 \times 10^7$ | 0.0276/0.0245 | 55 |
| $(iBA)_2(MA)_3Pb_4I_{13}$ film | 1.5 | 532 | N | 117 | 16/15 | 46 |
| $(OA)_2FA_{n-1}Pb_nBr_{3n+1}$ microplatelet | 9 | 442 | N | $3.2 \times 10^4$ | 0.25/1.45 | 45 |
| $EDA(MA)_3Pb_4I_{13}$ | 2 | 532 | Y | 125 | 0.41/0.38 | this work |

under a relatively large light intensity of 750 mW/cm$^2$. As compared with the EDA4 device in Group 1 that also consists of the quasi-2D perovskite channel with $n$ = 4, the photocurrent and photoresponsivity of the 0EDA device with the *i*BA spacer here are obviously smaller than those with the EDA spacer under the same light intensity. However, the on/off current ratio of the EDA4 device is smaller than that of 0EDA, which is because the relatively high conductivity induced the high dark current in the EDA4 detector. This further confirms that the short-chain bication EDA can indeed improve the photoresponse under high light intensity and enhance dark conductivity, as discussed above, as the two long-chain spacer cations in RPPs can block the conductivity of the perovskite heavily. At the same time, high-resolution $I-t$ curves of Group 2 devices are shown in Figures 5d and S10, where the rise and decay times are close to each other among all samples, being as low as about 400 $\mu$s. Overall, the excellent photodetection performance of these quasi-2D perovskite devices with EDA as the spacer cation (Group 1) and normal cation (Group 2) is evidently demonstrated. The EDA-based quasi-2D perovskite devices give the outstanding photoresponse characteristics, especially the response speed, which is in a distinct contrast to the ones with conventional single-cation spacers, such as *i*BA and BA.[41,46]

In addition to the conventional photodetectors demonstrated above, flexible photodetectors are even more charming because of their unique properties capable to attach onto any surface for many enabling applications.[47,48] In this work, the EDA-based quasi-2D perovskites with $n$ = 4 (i.e., EDA4 and Group 2 samples) are also fabricated on polyimide substrates for the construction of flexible photodetectors. For the performance assessment, it is important to evaluate the change in photocurrent as a function of the bending radius of all fabricated devices (Figure 6a). The optical image of the measurement setup is depicted to demonstrate the accurate control of the bending radius (Figure 6b inset). Based on the normalized photocurrent, it is observed that the photocurrent of the 0EDA device decreases rapidly to 23.5% of its initial value when the device is bent to a radius of 20 mm. Nevertheless, for the devices with low EDA content (i.e., $0.125 \leq x \leq 0.5$), their photocurrent remains at 73.6%, while the 1EDA device even maintains its photocurrent at 100% with the same bending magnitude. Once the devices are ultimately bent down to a radius of 2 mm, it is surprising that the photocurrent of EDA4 gradually increases to 177%. This excellent flexibility of EDA4 is anticipated to come from its unique bication spacers. For conventional spacer cations, there are two large organic layers sandwiched between two halide octahedron networks (i.e., one on the top and one at the bottom), where the binding of these organic bilayers comes from the weak van der Waals interaction (Figure 6c).[30,49] This weak van der Waals interaction can be easily broken by external forces;[32,50] therefore, the flexibility of typical RPPs is relatively poor with significant degradation in the photocurrent. On the other hand, when the bication EDA is used as the spacer cation in EDA4 to form the Dion–Jacobson phase, there is only one EDA layer acting as the spacer, without any van der Waals interaction discussed above, such that the flexibility can be greatly enhanced (Figure 6d). Also, the enhanced photocurrent behavior (i.e., with a photocurrent of >100%) can be attributed to the rougher surface induced by bending, leading to the improved light absorption because of the scattering of incident light. After that, the photocurrent is as well investigated as a function of the bending cycles to confirm the excellent mechanical flexibility of the EDA4 perovskite device (Figure 6d). All the different devices are bent for 10,000 cycles with a fixed minimum bending radius of 4 mm in each cycle. Obviously, the photocurrent of all Group 2 devices decreases rapidly during the first 1000 bending cycles. Excitingly, the photocurrent of the EDA4 detector remains above 100% within the entire 10,000 bending cycles, where the maximum value can even approach 200% of its initial value. This significant flexibility enhancement of the RPPs can make them promising for other advanced optoelectronic applications. In the future, further device optimization, such as utilizing flexible electrodes with proper thickness to achieve the more stable contact resistance, will be performed to minimize the photocurrent fluctuation during repeated bending cycles. In any case, all these results evidently indicate the photodetection performance of the EDA-based RPPs being superior, which is comparable with or even better than the RPPs reported in the recent literature (Table 1).

To further improve the performance of the perovskite-based photodetectors, a vertical device structure of the glass/indium tin oxide (ITO)/perovskite (EDA4)/Au detector was employed with the schematic shown in the inset of Figure S11b. Considering the same device dimension and illumination intensity, it is remarkable to observe that the photocurrent gets improved to 300 nA as compared with that (60 nA) of the glass/EDA4/Au device (Figures S11a and 4c). The responsivity and detectivity values are as well enhanced to 330 mA/W and $3 \times 10^{11}$ Jones, respectively (Figure S11c), together with efficient rise and decay times down to 169 and 68 $\mu$s, accordingly (Figure S11d). In fact, these device performance enhancements are mostly attributed to the more effective photocarrier separation and collection induced by the work function difference between ITO and Au electrodes, which are well recognized in other reports.[51,52]

Above and beyond the impressive device performance, the ambient stability of perovskite-based photodetectors is essential for their practical utilizations. In this case, the moisture stability of all fabricated devices is thoroughly


https://dx.doi.org/10.1021/acsami.0c09651
ACS Appl. Mater. Interfaces 2020, 12, 39567−39577

evaluated under a relative humidity of 60%. Table S1 compiles the change in the photocurrent of both Group 1 and Group 2 devices under a light intensity of 650 mW/cm$^2$ and a voltage of 2 V after storage in an ambient environment with a humidity of 60% for 7 days. It is found that the photocurrent of the 0EDA device (i.e., without any EDA content in the device channel) decreases to about 50% of its initial value after ambient storage for 7 days. For other devices in Group 1 and Group 2 that contain EDA as the spacer or normal cation, the degradation of their photocurrent is less than 15%, in which the photocurrent of several devices even increases slightly.

Actually, the enhanced photocurrent after ambient storage for a short time has been reported in other halide perovskites, where the enhancement can be due to the small concentration of perovskite decomposition products acting as dopants to contribute excess free carriers.[56−58] In parallel, XRD patterns of both fresh and aged samples are measured and shown in Figure S12. After ambient storage with a humidity of 60% for 7 days, the XRD spectra of all samples do not have any noticeable change, indicating the fairly good moisture stability of fabricated RPPs. However, after 30 days, the XRD patterns indicate that 0EDA, 0.5EDA, and 1EDA samples deteriorate in some extent, where an obvious peak of $PbI_2$ is observed. In contrast, the XRD spectra of 0.125EDA, 0.25EDA, and 0.375EDA samples almost remain the same, suggesting that a small amount of EDA can stabilize the crystal structure of RPPs.[24,27] This improved stability of EDA-based RPPs would further promote the device applications of halide perovskites.

## CONCLUSIONS

In summary, the synthesis of high-quality quasi-2D perovskite films has been successfully achieved via a one-step solution processing method, where the bication EDA is embedded into the perovskite structure as either the spacer cation or the normal cation or both. When EDA is utilized as the spacer cation to form the DJPs, the $EDA(MA)_{n-1}Pb_nI_{3n+1}$ film with $n$ = 4 exhibits the highest photoresponsibility of 125 mA/W under 532 nm irradiation. The response time of the films with $n$ = 2−4 is found to be as short as 400 $\mu$s. The great mechanical flexibility of these perovskite films is also observed, in which the photocurrent can even increase after bending to a radius of 2 mm and 10,000 bending cycles because of the unique binding nature of the DJPs with bication EDA as the spacer layer. For the case of employing EDA as the normal cation, different amounts of EDA can be exploited to substitute MA in the $(iBA)_2MA_3Pb_4I_{13}$ films (RPPs). It is important that the substitution of EDA can further improve the moisture stability of fabricated perovskite films. All these results can provide a valuable horizon to synthesize the optimal quasi-2D perovskite films for next-generation, mechanical, flexible, high-performance, and air-stable optoelectronic devices.

## EXPERIMENTAL SECTION

**Perovskite Precursor Synthesis.** For $EDA(MA)_{n-1}Pb_nI_{3n+1}$ films (Group 1 samples), where EDA acts as the spacer cation, $PbI_2$, $EDAI_2$, and MAI at a molar ratio of $n$:1:$n$ − 1 were dissolved in dimethylformamide (DMF). When n is fixed at 4, the $(iBA)_2(MA)_{3-2x}(EDA)_xPb_4I_{13}$ films (Group 2 samples), where EDA acts as the normal cation, $PbI_2$, $i$BAI, $EDAI_2$, and MAI at a molar ratio of 4:2:$x$:3 − 2$x$ were dissolved in DMF. The total $Pb^{2+}$ molar concentration was fixed at 1 M in the solution for all the precursor preparations. The solutions were then stirred at room temperature overnight.

**Device Fabrication.** The perovskite films were fabricated by a one-step spin-coating method in a nitrogen-filled glovebox, where the oxygen and moisture concentration were well controlled at the ppm level. Standard glass slides (15 mm × 15 mm × 0.7 mm) and PI substrates (25 mm × 10 mm × 0.1 mm) were first ultrasonically washed with acetone, ethanol, and deionized (DI) water for 15 min in succession, followed by a mild oxygen plasma treatment for 5 min (0.26 Torr, 30 W). In addition to these substrates, ITO/glass substrates were also employed with the 350 nm-thick ITO films (5 Ω/sq) predeposited onto the glass pieces (15 mm × 15 mm × 1 mm). After that, 60 $\mu$L of precursor solution was spin-coated on the glass or PI substrate at 3000 rpm for 30 s, subsequently with a thermal annealing at 100 °C for 10 min for the full crystallization of samples. The film thickness was controlled to about 400−500 nm, which was determined by SEM. Finally, with the assistance of a shadow mask, 80 nm-thick gold was thermally evaporated onto the films as electrodes. The channel length and width of the devices were determined to be 10 and 70 $\mu$m, respectively.

**Film and Device Characterization.** Surface morphologies of all the samples were characterized with SEM (FEI Quanta 450 FEG SEM) and AFM (Bruker Dimension Icon AFM). XRD (D2 Phaser with Cu K$\alpha$ radiation, Bruker) was used to evaluate the crystallinity and crystal structure of the obtained films. UV−vis absorption spectra were recorded using a PerkinElmer model Lambda 2S UV−VIS spectrometer. The PL spectra were acquired using a Hitachi F-4600 spectrophotometer with an excitation wavelength of 425 nm. The electrical performance of fabricated devices was characterized with a standard electrical probe station and an Agilent 4155C semiconductor analyzer (Agilent Technologies, California, USA). For photodetector measurement, a 532 nm laser diode was used as the light source for photodetector measurement, while the power of the incident irradiation was measured using a power meter (PM400, Thorlabs). An attenuator was also employed to tune the irradiation power illuminating on the device. A low noise current amplifier (SR570, Stanford Research Systems, USA) combined with a digital oscillator (TBS 1102B EDU, Tektronix, USA) is used to obtain the high-resolution current versus time curves to determine the response time of fabricated devices. The details of the experimental setup are depicted in Figure S13. All the measurements are conducted in a light-tight environment within a probe station in order to minimize the external disturbance.

## ASSOCIATED CONTENT

### Supporting Information

The Supporting Information is available free of charge at https://pubs.acs.org/doi/10.1021/acsami.0c09651.

FWHM in the XRD patterns, PL, SEM images, $I$−$V$ curves, EQE, detectivity, and high-resolution current versus time curves of the samples in Group 1 and Group 2; photoresponse properties of the "glass/ITO/EDA4/Au" device; photocurrents and XRD patterns of EDA4 and the samples in Group 2 after ambient storage with a humidity of 60%; and experimental setup for the photodetector measurement (PDF)

## AUTHOR INFORMATION

### Corresponding Author

**Johnny C. Ho** − *Department of Materials Science and Engineering, State Key Laboratory of Terahertz and Millimeter Waves, and Centre for Functional Photonics, City University of Hong Kong, Kowloon 999077, Hong Kong SAR, P. R. China; Key Laboratory of Advanced Materials Processing & Mold (Zhengzhou University), Ministry of Education, Zhengzhou 450002, P. R. China;* orcid.org/0000-0003-3000-8794; Email: johnnyho@cityu.edu.hk



https://dx.doi.org/10.1021/acsami.0c09651
ACS Appl. Mater. Interfaces 2020, 12, 39567−39577

## Authors

**Zhengxun Lai** − *Department of Materials Science and Engineering, City University of Hong Kong, Kowloon 999077, Hong Kong SAR, P. R. China*

**Ruoting Dong** − *Department of Materials Science and Engineering, City University of Hong Kong, Kowloon 999077, Hong Kong SAR, P. R. China*

**Qi Zhu** − *Department of Materials Science and Engineering, City University of Hong Kong, Kowloon 999077, Hong Kong SAR, P. R. China*

**You Meng** − *Department of Materials Science and Engineering, City University of Hong Kong, Kowloon 999077, Hong Kong SAR, P. R. China*

**Fei Wang** − *Department of Materials Science and Engineering, City University of Hong Kong, Kowloon 999077, Hong Kong SAR, P. R. China; State Key Laboratory of Luminescence and Applications, Changchun Institute of Optics, Fine Mechanics and Physics, Chinese Academy of Sciences, Changchun 130021, P. R. China*

**Fangzhou Li** − *Department of Materials Science and Engineering, City University of Hong Kong, Kowloon 999077, Hong Kong SAR, P. R. China*

**Xiuming Bu** − *Department of Materials Science and Engineering, City University of Hong Kong, Kowloon 999077, Hong Kong SAR, P. R. China;* orcid.org/0000-0002-2372-2271

**Xiaolin Kang** − *Department of Materials Science and Engineering, City University of Hong Kong, Kowloon 999077, Hong Kong SAR, P. R. China*

**Heng Zhang** − *Department of Materials Science and Engineering, City University of Hong Kong, Kowloon 999077, Hong Kong SAR, P. R. China*

**Quan Quan** − *Department of Materials Science and Engineering, City University of Hong Kong, Kowloon 999077, Hong Kong SAR, P. R. China*

**Wei Wang** − *Department of Materials Science and Engineering, City University of Hong Kong, Kowloon 999077, Hong Kong SAR, P. R. China*

**Feng Wang** − *Department of Materials Science and Engineering, City University of Hong Kong, Kowloon 999077, Hong Kong SAR, P. R. China;* orcid.org/0000-0001-9471-4386

**SenPo Yip** − *Department of Materials Science and Engineering, State Key Laboratory of Terahertz and Millimeter Waves, and Centre for Functional Photonics, City University of Hong Kong, Kowloon 999077, Hong Kong SAR, P. R. China*

Complete contact information is available at: https://pubs.acs.org/10.1021/acsami.0c09651


## Author Contributions

The manuscript was written through contributions of all authors. All authors have given approval to the final version of the manuscript.

## Notes

The authors declare no competing financial interest.

## ■ ACKNOWLEDGMENTS

We acknowledge the General Research Fund (CityU 11204618) and the Theme-based Research (T42-103/16-N) of the Research Grants Council of Hong Kong SAR, China, the National Natural Science Foundation of China (Grant 51672229), the Science Technology and Innovation Committee of Shenzhen Municipality (Grant JCYJ20170818095520778), and a grant from the Shenzhen Research Institute, City University of Hong Kong.

## ■ REFERENCES


(1) Jung, H. S.; Park, N.-G. Perovskite Solar Cells: From Materials to Devices. *Small* **2015**, *11*, 10−25.

(2) Lian, Z.; Yan, Q.; Lv, Q.; Wang, Y.; Liu, L.; Zhang, L.; Pan, S.; Li, Q.; Wang, L.; Sun, J.-L. High-Performance Planar-Type Photodetector on (100) Facet of MAPbI3 Single Crystal. *Sci. Rep.* **2015**, *5*, 1−10.

(3) Liu, J.; Xue, Y.; Wang, Z.; Xu, Z.-Q.; Zheng, C.; Weber, B.; Song, J.; Wang, Y.; Lu, Y.; Zhang, Y.; Bao, Q. Two-Dimensional $CH_3NH_3PbI_3$ Perovskite: Synthesis and Optoelectronic Application. *ACS Nano* **2016**, *10*, 3536−3542.

(4) Ma, C.; Shi, Y.; Hu, W.; Chiu, M. H.; Liu, Z.; Bera, A.; Li, F.; Wang, H.; Li, L. J.; Wu, T. Heterostructured $WS_2/CH_3NH_3PbI_3$ Photoconductors with Suppressed Dark Current and Enhanced Photodetectivity. *Adv. Mater.* **2016**, *28*, 3683−3689.

(5) Najafi, L.; Taheri, B.; Martín-García, B.; Bellani, S.; Di Girolamo, D.; Agresti, A.; Oropesa-Nunìez, R.; Pescetelli, S.; Vesce, L.; Calabrò, E.; Prato, M.; Del Rio Castillo, A. E.; Di Carlo, A.; Bonaccorso, F. $MoS_2$ Quantum Dot/Graphene Hybrids for Advanced Interface Engineering of a $CH_3NH_3PbI_3$ Perovskite Solar Cell with an Efficiency of over 20%. *ACS Nano* **2018**, *12*, 10736−10754.

(6) Lai, Q.; Zhu, L.; Pang, Y.; Xu, L.; Chen, J.; Ren, Z.; Luo, J.; Wang, L.; Chen, L.; Han, K.; Lin, P.; Li, D.; Lin, S.; Chen, B.; Pan, C.; Wang, Z. L. Piezo-Phototronic Effect Enhanced Photodetector Based on $CH_3NH_3PbI_3$ Single Crystals. *ACS Nano* **2018**, *12*, 10501−10508.

(7) Correa-Baena, J.-P.; Saliba, M.; Buonassisi, T.; Grätzel, M.; Abate, A.; Tress, W.; Hagfeldt, A. Promises and Challenges of Perovskite Solar Cells in Portable Applications. *Science* **2017**, *358*, 739−744.

(8) Xie, C.; Liu, C. K.; Loi, H. L.; Yan, F. Perovskite-Based Phototransistors and Hybrid Photodetectors. *Adv. Funct. Mater.* **2019**, *30*, 1903907.

(9) Lin, R.; Xiao, K.; Qin, Z.; Han, Q.; Zhang, C.; Wei, M.; Saidaminov, M. I.; Gao, Y.; Xu, J.; Xiao, M.; Li, A.; Zhu, J.; Sargent, E. H.; Tan, H. Monolithic All-Perovskite Tandem Solar Cells with 24.8% Efficiency Exploiting Comproportionation to Suppress Sn(II) Oxidation in Precursor Ink. *Nat. Energy* **2019**, *4*, 864−873.

(10) Xu, J.; Boyd, C. C.; Yu, Z. J.; Palmstrom, A. F.; Witter, D. J.; Larson, B. W.; France, R. M.; Werner, J.; Harvey, S. P.; Wolf, E. J.; Weigand, W.; Manzoor, S.; Van Hest, M. F. A. M.; Berry, J. J.; Luther, J. M.; Holman, Z. C.; McGehee, M. D. Triple-Halide Wide-Band Gap Perovskites with Suppressed Phase Segregation for Efficient Tandems. *Scienc* **2020**, *367*, 1097−1104.

(11) Kim, D.; Jung, H. J.; Park, I. J.; Larson, B. W.; Dunfield, S. P.; Xiao, C.; Kim, J.; Tong, J.; Boonmongkolras, P.; Ji, S. G.; Zhang, F.; Pae, S. R.; Kim, M.; Kang, S. B.; Dravid, V.; Berry, J. J.; Kim, J. Y.; Zhu, K.; Kim, D. H.; Shin, B. Efficient, Stable Silicon Tandem Cells Enabled by Anion-Engineered Wide-Bandgap Perovskites. *Science* **2020**, *368*, 155−160.

(12) Hou, Y.; Aydin, E.; De Bastiani, M.; Xiao, C.; Isikgor, F. H.; Xue, D.-J.; Chen, B.; Chen, H.; Bahrami, B.; Chowdhury, A. H.; Johnston, A.; Baek, S.-W.; Huang, Z.; Wei, M.; Dong, Y.; Troughton, J.; Jalmood, R.; Mirabelli, A. J.; Allen, T. G.; Van Kerschaver, E.; Saidaminov, M. I.; Baran, D.; Qiao, Q.; Zhu, K.; De Wolf, S.; Sargent, E. H. Efficient Tandem Solar Cells with Solution-Processed Perovskite on Textured Crystalline Silicon. *Science* **2020**, *367*, 1135−1140.

(13) Niu, G.; Guo, X.; Wang, L. Review of Recent Progress in Chemical Stability of Perovskite Solar Cells. *J. Mater. Chem. A* **2015**, *3*, 8970−8980.

(14) Conings, B.; Drijkoningen, J.; Gauquelin, N.; Babayigit, A.; D'Haen, J.; D'Olieslaeger, L.; Ethirajan, A.; Verbeeck, J.; Manca, J.; Mosconi, E.; Angelis, F. D.; Boyen, H.-G. Intrinsic Thermal Instability of Methylammonium Lead Trihalide Perovskite. *Adv. Energy Mater.* **2015**, *5*, 1500477−8.

(15) Dou, L.; Wong, A. B.; Yu, Y.; Lai, M.; Kornienko, N.; Eaton, S. W.; Fu, A.; Bischak, C. G.; Ma, J.; Ding, T.; Ginsberg, N. S.; Wang, L.-W.; Alivisatos, A. P.; Yang, P. Atomically Thin Two-Dimensional Organic-Inorganic Hybrid Perovskites. *Science* **2015**, *349*, 1518−1521.
(16) Liang, D.; Peng, Y.; Fu, Y.; Shearer, M. J.; Zhang, J.; Zhai, J.; Zhang, Y.; Hamers, R. J.; Andrew, T. L.; Jin, S. Color-Pure Violet-Light-Emitting Diodes Based on Layered Lead Halide Perovskite Nanoplates. *ACS Nano* **2016**, *10*, 6897−6904.
(17) Chen, Y.; Sun, Y.; Peng, J.; Tang, J.; Zheng, K.; Liang, Z. 2D Ruddlesden−Popper Perovskites for Optoelectronics. *Adv. Mater.* **2018**, *30*, 1703487.
(18) Shi, E.; Gao, Y.; Finkenauer, B. P.; Akriti, A.; Coffey, A. H.; Dou, L. Two-Dimensional Halide Perovskite Nanomaterials and Heterostructures. *Chem. Soc. Rev.* **2018**, *47*, 6046−6072.
(19) Kagan, C. R.; Mitzi, D. B.; Dimitrakopoulos, C. D. Organic-Inorganic Hybrid Materials as Semiconducting Channels in Thin-Film Field-Effect Transistors. *Science* **1999**, *286*, 945−947.
(20) Stoumpos, C. C.; Cao, D. H.; Clark, D. J.; Young, J.; Rondinelli, J. M.; Jang, J. I.; Hupp, J. T.; Kanatzidis, M. G. Ruddlesden-Popper Hybrid Lead Iodide Perovskite 2D Homologous Semiconductors. *Chem. Mater.* **2016**, *28*, 2852−2867.
(21) Smith, I. C.; Hoke, E. T.; Solis-Ibarra, D.; McGehee, M. D.; Karunadasa, H. I. A Layered Hybrid Perovskite Solar-Cell Absorber with Enhanced Moisture Stability. *Angew. Chem., Int. Ed.* **2014**, *53*, 11232−11235.
(22) Cao, D. H.; Stoumpos, C. C.; Yokoyama, T.; Logsdon, J. L.; Song, T.-B.; Farha, O. K.; Wasielewski, M. R.; Hupp, J. T.; Kanatzidis, M. G. Thin Films and Solar Cells Based on Semiconducting Two-Dimensional Ruddlesden-Popper $(CH_3(CH_2)_3NH_3)_2(CH_3NH_3)_{n-1}Sn_nI_{3n+1}$ Perovskites. *ACS Energy Lett.* **2017**, *2*, 982−990.
(23) Hu, J.; Yan, L.; You, W. Two-Dimensional Organic−Inorganic Hybrid Perovskites: A New Platform for Optoelectronic Applications. *Adv. Mater.* **2018**, *30*, 1802041.
(24) Zhang, T.; Dar, M. I.; Li, G.; Xu, F.; Guo, N.; Grätzel, M.; Zhao, Y. Bication Lead Iodide 2D Perovskite Component to Stabilize Inorganic $\alpha$-$CsPbI_3$ Perovskite Phase for High-Efficiency Solar Cells. *Sci. Adv.* **2017**, *3*, No. e1700841.
(25) Lemmerer, A.; Billing, D. G. Lead Halide Inorganic-Organic Hybrids Incorporating Diammonium Cations. *CrystEngComm* **2012**, *14*, 1954−1966.
(26) Chen, Z.; Zheng, X.; Yao, F.; Ma, J.; Tao, C.; Fang, G. Methylammonium, Formamidinium and Ethylenediamine Mixed Triple-Cation Perovskite Solar Cells with High Efficiency and Remarkable Stability. *J. Mater. Chem. A* **2018**, *6*, 17625−17632.
(27) Lu, J.; Jiang, L.; Li, W.; Li, F.; Pai, N. K.; Scully, A. D.; Tsai, C.-M.; Bach, U.; Simonov, A. N.; Cheng, Y.-B.; Spiccia, L. Diammonium and Monoammonium Mixed-Organic-Cation Perovskites for High Performance Solar Cells with Improved Stability. *Adv. Energy Mater.* **2017**, *7*, 1700444−10.
(28) Daub, M.; Hillebrecht, H. Tailoring the Band Gap in 3D Hybrid Perovskites by Substitution of the Organic Cations: $(CH_3NH_3)_{1-2y}(NH_3(CH_2)_2NH_3)_{2y}Pb_{1-y}I_3$ $(0\leq y\leq 0.25)$. *Chem.—Eur. J.* **2018**, *24*, 9075−9082.
(29) Krishnamurthy, S.; Naphade, R.; Mir, W. J.; Gosavi, S.; Chakraborty, S.; Vaidhyanathan, R.; Ogale, S. Molecular and Self-Trapped Excitonic Contributions to the Broadband Luminescence in Diamine-Based Low-Dimensional Hybrid Perovskite Systems. *Adv. Opt. Mater.* **2018**, *6*, 1800751.
(30) Xu, Z.; Chen, M.; Liu, S. F. First-Principles Study of Enhanced Out-of-Plane Transport Properties and Stability in Dion-Jacobson Two-Dimensional Perovskite Semiconductors for High-Performance Solar Cell Applications. *J. Phys. Chem. Lett.* **2019**, *10*, 3670−3675.
(31) Niu, W.; Eiden, A.; Vijaya Prakash, G.; Baumberg, J. J. Exfoliation of Self-Assembled 2D Organic-Inorganic Perovskite Semiconductors. *Appl. Phys. Lett.* **2014**, *104* (). https://doi.org/DOI: 10.1063/1.4874846.
(32) Blancon, J.-C.; Tsai, H.; Nie, W.; Stoumpos, C. C.; Pedesseau, L.; Katan, C.; Kepenekian, M.; Soe, C. M. M.; Appavoo, K.; Sfeir, M. Y.; Tretiak, S.; Ajayan, P. M.; Kanatzidis, M. G.; Even, J.; Crochet, J. J.; Mohite, A. D. Extremely Efficient Internal Exciton Dissociation through Edge States in Layered 2D Perovskites. *Science* **2017**, *355*, 1288−1292.
(33) Dong, R.; Lan, C.; Li, F.; Yip, S.; Ho, J. C. Incorporating Mixed Cations in Quasi-2D Perovskites for High-Performance and Flexible Photodetectors. *Nanoscale Horiz.* **2019**, *4*, 1342−1352.
(34) Lan, C.; Zhou, Z.; Wei, R.; Ho, J. C. Two-Dimensional Perovskite Materials: From Synthesis to Energy-Related Applications. *Mater. Today Energy* **2019**, *11*, 61−82.
(35) Liu, J.; Leng, J.; Wu, K.; Zhang, J.; Jin, S. Observation of Internal Photoinduced Electron and Hole Separation in Hybrid Two-Dimentional Perovskite Films. *J. Am. Chem. Soc.* **2017**, *139*, 1432−1435.
(36) Qing, J.; Liu, X.-K.; Li, M.; Liu, F.; Yuan, Z.; Tiukalova, E.; Yan, Z.; Duchamp, M.; Chen, S.; Wang, Y.; Bai, S.; Liu, J.-M.; Snaith, H. J.; Lee, C.-S.; Sum, T. C.; Gao, F. Aligned and Graded Type-II Ruddlesden−Popper Perovskite Films for Efficient Solar Cells. *Adv. Energy Mater.* **2018**, *8*, 1800185.
(37) Bi, C.; Wang, Q.; Shao, Y.; Yuan, Y.; Xiao, Z.; Huang, J. Non-Wetting Surface-Driven High-Aspect-Ratio Crystalline Grain Growth for Efficient Hybrid Perovskite Solar Cells. *Nat. Commun.* **2015**, *6*, 7747.
(38) Lai, Z.; Li, Z.; Liu, X.; Bai, L.; Tian, Y.; Mi, W. Ferromagnetic Resonance of Facing-Target Sputtered Epitaxial $\gamma'$-$Fe_4N$ Films: The Influence of Thickness and Substrates. *J. Phys. D: Appl. Phys.* **2018**, *51*, 245001.
(39) Lan, C.; Dong, R.; Zhou, Z.; Shu, L.; Li, D.; Yip, S.; Ho, J. C. Large-Scale Synthesis of Freestanding Layer-Structured $PbI_2$ and $MAPbI_3$ Nanosheets for High-Performance Photodetection. *Adv. Mater.* **2017**, *29*, 1702759.
(40) Binet, F.; Duboz, J. Y.; Rosencher, E.; Scholz, F.; Härle, V. Mechanisms of Recombination in GaN Photodetectors. *Appl. Phys. Lett.* **1996**, *69*, 1202−1204.
(41) Zhou, J.; Chu, Y.; Huang, J. Photodetectors Based on Two-Dimensional Layer-Structured Hybrid Lead Iodide Perovskite Semiconductors. *ACS Appl. Mater. Interfaces* **2016**, *8*, 25660−25666.
(42) Tong, X.-W.; Kong, W.-Y.; Wang, Y.-Y.; Zhu, J.-M.; Luo, L.-B.; Wang, Z.-H. High-Performance Red-Light Photodetector Based on Lead-Free Bismuth Halide Perovskite Film. *ACS Appl. Mater. Interfaces* **2017**, *9*, 18977−18985.
(43) Meng, Y.; Lan, C.; Li, F.; Yip, S.; Wei, R.; Kang, X.; Bu, X.; Dong, R.; Zhang, H.; Ho, J. C. Direct Vapor-Liquid-Solid Synthesis of All-Inorganic Perovskite Nanowires for High-Performance Electronics and Optoelectronics. *ACS Nano* **2019**, *13*, 6060−6070.
(44) Zhu, B.-S.; He, Z.; Yao, J.-S.; Chen, C.; Wang, K.-H.; Yao, H.-B.; Liu, J.-W.; Yu, S.-H. Potassium Ion Assisted Synthesis of Organic−Inorganic Hybrid Perovskite Nanobelts for Stable and Flexible Photodetectors. *Adv. Opt. Mater.* **2018**, *6*, 1701029.
(45) Yu, D.; Cao, F.; Shen, Y.; Liu, X.; Zhu, Y.; Zeng, H. Dimensionality and Interface Engineering of 2D Homologous Perovskites for Boosted Charge-Carrier Transport and Photodetection Performances. *J. Phys. Chem. Lett.* **2017**, *8*, 2565−2572.
(46) Dong, R.; Lan, C.; Xu, X.; Liang, X.; Hu, X.; Li, D.; Zhou, Z.; Shu, L.; Yip, S.; Li, C.; Tsang, S.-W.; Ho, J. C. Novel Series of Quasi-2D Ruddlesden−Popper Perovskites Based on Short-Chained Spacer Cation for Enhanced Photodetection. *ACS Appl. Mater. Interfaces* **2018**, *10*, 19019−19026.
(47) Cao, F.; Tian, W.; Wang, M.; Cao, H.; Li, L. Semitransparent, Flexible, and Self-Powered Photodetectors Based on Ferroelectricity-Assisted Perovskite Nanowire Arrays. *Adv. Funct. Mater.* **2019**, *29*, 1901280.
(48) Zhu, T.; Yang, Y.; Zheng, L.; Liu, L.; Becker, M. L.; Gong, X. Solution-Processed Flexible Broadband Photodetectors with Solution-Processed Transparent Polymeric Electrode. *Adv. Funct. Mater.* **2020**, *30*, 1909487.
(49) Ha, S. T.; Liu, X.; Zhang, Q.; Giovanni, D.; Sum, T. C.; Xiong, Q. Synthesis of Organic-Inorganic Lead Halide Perovskite Nano-

platelets: Towards High-Performance Perovskite Solar Cells and Optoelectronic Devices. *Adv. Opt. Mater.* **2014**, *2*, 838−844.
(50) Niu, W.; Eiden, A.; Vijaya Prakash, G.; Baumberg, J. J. Exfoliation of Self-Assembled 2D Organic-Inorganic Perovskite Semiconductors. *Appl. Phys. Lett.* **2014**, *104*, 171111.
(51) Shaikh, P. A.; Shi, D.; Retamal, J. R. D.; Sheikh, A. D.; Haque, M. A.; Kang, C.-F.; He, J.-H.; Bakr, O. M.; Wu, T. Schottky Junctions on Perovskite Single Crystals: Light-Modulated Dielectric Constant and Self-Biased Photodetection. *J. Mater. Chem. C* **2016**, *4*, 8304−8312.
(52) Dai, M.; Chen, H.; Wang, F.; Long, M.; Shang, H.; Hu, Y.; Li, W.; Ge, C.; Zhang, J.; Zhai, T.; Fu, Y.; Hu, P. Ultrafast and Sensitive Self-Powered Photodetector Featuring Self-Limited Depletion Region and Fully Depleted Channel with van Der Waals Contacts. *ACS Nano* **2020**, *14*, 9098.
(53) Chen, J.; Wang, Y.; Gan, L.; He, Y.; Li, H.; Zhai, T. Generalized Self-Doping Engineering towards Ultrathin and Large-Sized Two-Dimensional Homologous Perovskites. *Angew. Chem., Int. Ed.* **2017**, *56*, 14893−14897.
(54) Zhang, Y.; Liu, Y.; Xu, Z.; Ye, H.; Li, Q.; Hu, M.; Yang, Z.; Liu, S. Two-Dimensional $(PEA)_2PbBr_4$ Perovskite Single Crystals for a High Performance UV-Detector. *J. Mater. Chem. C* **2019**, *7*, 1584−1591.
(55) Feng, J.; Gong, C.; Gao, H.; Wen, W.; Gong, Y.; Jiang, X.; Zhang, B.; Wu, Y.; Wu, Y.; Fu, H.; Jiang, L.; Zhang, X. Single-Crystalline Layered Metal-Halide Perovskite Nanowires for Ultrasensitive Photodetectors. *Nat. Electron.* **2018**, *1*, 404−410.
(56) Zhang, B.; Bi, W.; Wu, Y.; Chen, C.; Li, H.; Song, Z.; Dai, Q.; Xu, L.; Song, H. High-Performance $CsPbIBr_2$ Perovskite Solar Cells: Effectively Promoted Crystal Growth by Antisolvent and Organic Ion Strategies. *ACS Appl. Mater. Interfaces* **2019**, *11*, 33868−33878.
(57) Peng, W.; Yin, J.; Ho, K.-T.; Ouellette, O.; De Bastiani, M.; Murali, B.; El Tall, O.; Shen, C.; Miao, X.; Pan, J.; Alarousu, E.; He, J.-H.; Ooi, B. S.; Mohammed, O. F.; Sargent, E.; Bakr, O. M. Ultralow Self-Doping in Two-Dimensional Hybrid Perovskite Single Crystals. *Nano Lett.* **2017**, *17*, 4759−4767.
(58) Chen, S.; Teng, C.; Zhang, M.; Li, Y.; Xie, D.; Shi, G. A Flexible UV−Vis−NIR Photodetector Based on a Perovskite/Conjugated-Polymer Composite. *Adv. Mater.* **2016**, *28*, 5969−5974.


https://dx.doi.org/10.1021/acsami.0c09651
*ACS Appl. Mater. Interfaces* 2020, 12, 39567−39577